PHYSICAL REVIEW A **109**, 053315 (2024)

Blocking particle dynamics in a diamond chain with spatially increasing flux

Tomonari Mizoguchi,[1,*] Yoshihito Kuno,[2] and Yasuhiro Hatsugai[1]
[1]*Department of Physics, University of Tsukuba, Tsukuba, Ibaraki 305-8571, Japan*
[2]*Graduate School of Engineering Science, Akita University, Akita 010-8502, Japan*

(Received 23 August 2023; accepted 2 May 2024; published 22 May 2024)

Spatial nonuniformity in tight-binding models serves as a source of rich phenomena. In this paper we study a diamond-chain tight-binding model with a spatially increasing magnetic flux at each plaquette. In the numerical studies with various combinations of the minimum and maximum flux values, we find the characteristic dynamics of a particle, namely, a particle slows down when approaching the plaquette with π flux. This originates from the fact that the sharply localized eigenstates exist around the π-flux plaquette. These localized modes can be understood from a squared model of the original one. This characteristic blocked dynamics can be observed in photonic waveguides or cold atoms.

DOI: 10.1103/PhysRevA.109.053315

I. INTRODUCTION

The dynamics of particles in tight-binding models has attracted considerable interest. The particle dynamics contains a variety of useful information about the properties of the systems, such as the localized nature [1] and nontrivial topology [2–11]. It also provides a novel notion based on the dynamical properties [12–14]. Moreover, such dynamical properties have become experimentally accessible. The tight-binding-type models were originally introduced to describe the electronic structures in solid. Recently, it has been recognized that tight-binding models describe various systems having discrete translational symmetry, such as ultracold atoms in an optical lattice [15–18], light in photonic waveguides [19,20], and wave motion in mechanical systems [21,22].

The roles of spatial modulations of Hamiltonians in wave functions and dynamics have also attracted considerable interest. One of the most well-known phenomena induced by the spatial modulation is Anderson localization [23–25], where disorders turn extended wave functions into exponentially localized ones. The drastic change of the wave functions is also caused by disorder-free modulations. For instance, a uniform electric field that causes a linear potential induces the localization of the wave functions, which is called the Wannier-Stark localization [26]. Then the resulting dynamics becomes oscillatory rather than accelerated. This oscillation of the particle dynamics, called Bloch oscillation, has been experimentally realized in various artificial setups [27,28]. Recently, the roles of the characteristic band structures and Bloch wave functions, such as Dirac fermions and flat bands, in the aforementioned electric-field-induced phenomena have been investigated extensively [29–32].

In this paper we seek another disorder-free modulation of Hamiltonians that causes the characteristic dynamics of tight-binding models. Specifically, we introduce the diamond-chain model with a spatially increasing flux. The diamond chain is a one-dimensional corner-sharing network of square plaquettes (Fig. 1). In the tight-binding models of this lattice, we can introduce the flux at each plaquette as a Peierls phase. In fact, the effects of the uniform flux in the diamond chain have been studied intensively. When the flux is equal to π (per flux quantum), all the bands become completely dispersionless, resulting in the complete confinement of the particle motion. Such a flux-induced localization, called an Aharonov-Bohm cage [33–40], has been experimentally realized in various setups such as photonic crystals [41–43], ultracold atoms [44] superconducting circuits [45] and *LC* circuits [46,47]. (We summarize the characteristic band structures for the uniform flux case in Appendix A.)

In the present work we consider the case where the fluxes penetrating the leftmost and rightmost plaquettes are Φ_{min} and Φ_{max}, respectively, and the flux between them is increased linearly. We investigate the characteristic localization and dynamics of this model. We first investigate the case of $(\Phi_{\mathrm{min}}, \Phi_{\mathrm{max}}) = (0, \pi)$. We reveal that the eigenstates can be categorized into several types. Among them, we find that sharply localized eigenstates near the π-flux plaquette appear whose energy is close to the finite-energy flat band in the uniform π-flux case. We also investigate the single-particle dynamics where the particle is initially localized at one or a few sites. We find a characteristic feature of the wave front, namely, the particle slows down as it approaches the π-flux plaquette. Remarkably, this behavior resembles neither the ballistic motion of the uniform system nor the Bloch oscillation in the linear potential. On the basis of these results, we further study the cases of various choices of Φ_{min} and Φ_{max}. We find that the localized states around the π-flux plaquette appear ubiquitously and such states serve as a blockade of the particle dynamics.

The rest of this paper is structured as follows. In Sec. II we introduce our model and its basics such as symmetries. Our main results of this work are presented in Sec. III. We

---

[*] mizoguchi@rhodia.ph.tsukuba.ac.jp

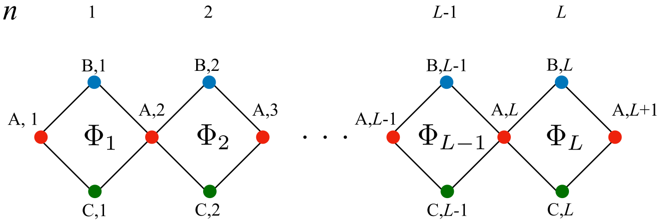

FIG. 1. Schematic of the diamond-chain model with spatially increasing flux.

study in detail the cases where the flux is increased from 0 to π and from 0 to 2π. Based on these results, we discuss the particle dynamics of various combinations of Φ_{min} and Φ_{max}. Section IV is devoted to a comparison between the diamond-chain model and the other models with increasing magnetic flux to elucidate the uniqueness and ubiquity of the diamond chain. We also address another aspect of the characteristic dynamics, namely, the early-time dynamics. We present a summary of this paper and several perspectives for future work in Sec. V.

II. MODEL

We study the tight-binding Hamiltonian

$$H=\sum_{n=1}^{L} c^{\dagger}_{A,n}(c_{B,n}+c_{C,n})+c^{\dagger}_{A,n+1}(e^{-i\Phi_n}c_{B,n}+c_{C,n})+\text{H.c.}, \tag{1}$$

where $c_{A,n}$, $c_{B,n}$, and $c_{C,n}$ are annihilation operators and Φ_n is a spatial-dependent flux. Note that we focus on the open boundary case and the total number of sites is $N_{\text{site}}=3L+1$. For convenience, we introduce the matrix representation of this Hamiltonian

$$H=\hat{\boldsymbol{c}}^{\dagger}\mathcal{H}\hat{\boldsymbol{c}}, \tag{2}$$

where $\hat{\boldsymbol{c}}$ is the column vector of the annihilation operator and $\mathcal{H}$ is the Hamiltonian matrix. The $\mathcal{H}$ preserves the chiral symmetry, namely, $\mathcal{H}$ satisfies $g\mathcal{H}g=-\mathcal{H}$, where

$$[g]_{ij}=g_i\delta_{i,j}, \tag{3}$$

with $g_i=+1$ (-1) for $i\in A$ $(i\in B, C)$. By diagonalizing the Hamiltonian, we have

$$H=\sum_{\nu}\varepsilon_{\nu}\alpha^{\dagger}_{\nu}\alpha_{\nu}, \tag{4}$$

where

$$\alpha^{\dagger}_{\nu}=\sum_{i}\psi^{\nu}(i)c^{\dagger}_{i} \tag{5}$$

is the creation operator of the νth eigenstate, α_ν is its Hermitian conjugate, and $\psi^{\nu}(i)$ is the wave function at site i.

In the following, we study the case of spatially increasing flux. Specifically, we set $\Phi_n=\Phi_{\text{min}}+\Delta\Phi(n-1)$, with $\Delta\Phi:=\frac{\Phi_{\text{max}}-\Phi_{\text{min}}}{L-1}$. This situation induces a different strength of flux for each plaquette in the system, as shown in Fig. 1. Before proceeding to the numerical results of various $(\Phi_{\text{min}},\Phi_{\text{max}})$, we address the generic properties of the eigenvalues and eigenstates. First, the chiral symmetry of $\mathcal{H}$ indicates that the positive- and negative-energy modes appear in a pairwise manner and that there exist degenerate zero-energy modes, whose number is equal to $|\text{Tr}(g)|=(L-1)$ [48–51]. In fact, the degenerate zero-energy modes are spanned by the compact localized states, shown in Appendix B.

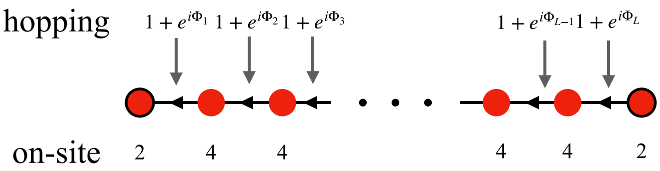

FIG. 2. Schematic of the Hamiltonian h^A.

Second, the chiral symmetry also indicates that taking a square of the Hamiltonian provides a perspective on the finite-energy modes [42,52–59]. If we align the basis $\hat{\boldsymbol{c}}$ as $\hat{\boldsymbol{c}}=(c_{A,1},\dots,c_{A,L+1},c_{B,1},\dots,c_{B,L},c_{C,1},\dots,c_{C,L})^{\text{T}}$, we can write the Hamiltonian matrix in the form

$$\mathcal{H}=\begin{pmatrix}\mathcal{O}_{L+1,L+1} & \Omega^{\dagger}\\ \Omega & \mathcal{O}_{2L,2L}\end{pmatrix}, \tag{6}$$

where $\mathcal{O}_{M_1,M_2}$ stands for the $M_1\times M_2$ zero matrix and Ω is the $2L\times(L+1)$ matrix that describes the hopping between A sites and B or C sites. Taking the square of $\mathcal{H}$, we have

$$\mathcal{H}^2=\begin{pmatrix}h^A & \mathcal{O}_{L+1,2L}\\ \mathcal{O}_{2L,L+1} & h^{B,C}\end{pmatrix}, \tag{7}$$

where $h^A:=\Omega^{\dagger}\Omega$ and $h^{B,C}:=\Omega\Omega^{\dagger}$. Let $\boldsymbol{u}_\nu$ be a normalized eigenvector of h^A with an eigenvalue E_ν. Since h^A is positive semidefinite, $E_\nu\geqslant 0$ holds. In the following, we assume that $E_\nu>0$. Then we find the following two facts: (i) The vector $\boldsymbol{u}'_\nu=\frac{1}{\sqrt{E_\nu}}\Omega\boldsymbol{u}_\nu$ is a normalized eigenvector of $h^{B,C}$ and (ii) the vector $\boldsymbol{\psi}^{\pm}_{\nu}=\frac{1}{\sqrt{2}}(\boldsymbol{u}_\nu,\pm\boldsymbol{u}'_\nu)^{\text{T}}$ is an eigenvector of $\mathcal{H}$ with an eigenvalue $\pm\sqrt{E}$ [55,59,60]. The above facts, in combination with an additional fact that the matrix elements of Ω are restricted to pairs of neighboring sites, indicate the following: If $\boldsymbol{u}_\nu$ is a sharply localized wave function, so are $\boldsymbol{u}'_\nu$ and $\boldsymbol{\psi}^{\pm}_{\nu}$. Let us focus on h^A, which corresponds to a tight-binding Hamiltonian of the $(L+1)$-site chain. In Fig. 2 we show the schematic of h^A. It contains the on-site potentials and the nearest-neighbor hoppings. In particular, the hopping parameter between the nth site and the $(n+1)$th site is given by $t_{n,n+1}=t^{*}_{n+1,n}=1+e^{i\Phi_n}$. This indicates the following. Suppose there exists a plaquette whose flux value is close to π, i.e., $\Phi_n=\pi+\delta\Phi$, with $\delta\Phi$ a small number. Then the hopping parameter is approximated as $t_{n,n+1}\sim -i\delta\Phi$. This means that the hoppings for h^A near n corresponding to the π-flux plaquette are largely suppressed, which gives rise to a sharply localized eigenstate $\boldsymbol{u}_\nu$ (but its state does not have compact support due to the small finite contribution of hopping $-i\delta\Phi$ around the π-flux plaquette). Turning to the diamond chain, the resulting $\boldsymbol{\psi}^{\pm}_{\nu}$ around the π-flux plaquette is sharply localized too, as we will see in the next section.

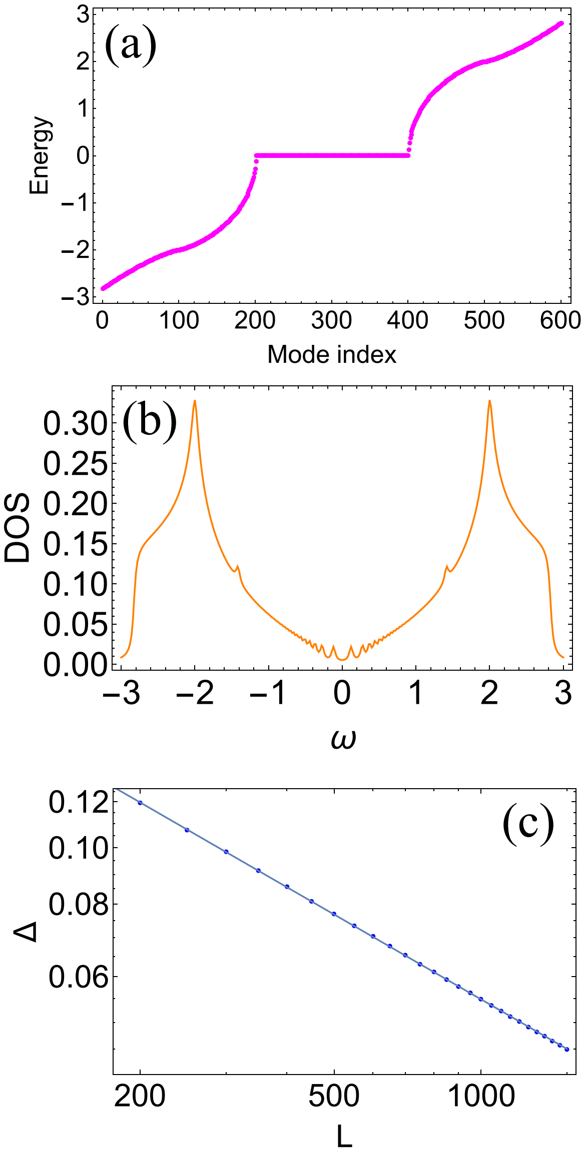

FIG. 3. (a) Energy spectrum and (b) DOS for $(\Phi_{\min}, \Phi_{\max}) = (0, \pi)$, $L = 200$. In (b) the contribution from the degenerate zero-energy modes is excluded. (c) Gap between the zero-energy mode and the lowest positive-energy mode, Δ, as a function of L.

III. RESULTS

In this section we present our numerical results on the diamond-chain model for various combinations of $(\Phi_{\min}, \Phi_{\max})$.

A. Case of $(\Phi_{\min}, \Phi_{\max}) = (0, \pi)$

We first focus on the case of $(\Phi_{\min}, \Phi_{\max}) = (0, \pi)$. In fact, the detailed analysis of this case is helpful for understanding the generic cases of $(\Phi_{\min}, \Phi_{\max})$. In particular, the role of the π-flux plaquette is elucidated.

We first study the energy spectrum and energy eigenstates. In Fig. 3(a) we plot the energy spectrum. We see that the zero-energy modes are macroscopically degenerate, as we mentioned in the preceding section.

In Fig. 3(b) we plot the density of states (DOS) for the nonzero energy modes, defined as

$$\mathrm{DOS}(\omega) = -\frac{1}{\pi N_{\mathrm{site}}} \sum_{\nu \neq \text{zero modes}} \mathrm{Im}\left(\frac{1}{\omega + i\eta - \varepsilon_\nu}\right). \tag{8}$$

Here η is a small parameter set as $\eta = 0.03$ so that the DOS becomes reasonably smooth as a function of ω. As indicated in Eq. (8), we exclude the degenerate zero-energy modes that give a divergent contribution to the DOS near $\omega = 0$, in order to clarify the contribution from nonzero-energy modes. We see that the DOS drops around $\omega = 0$. We also see the large DOS around $\omega = \pm 2$, which corresponds to the energy of the perfect flat bands for the π-flux case (see Appendix A).

The drop of the DOS around $\omega = 0$ raises the question whether the first excited state above the zero-energy modes, i.e., the $(2L+1)$th mode, has a finite-energy gap or not. To see this, in Fig. 3(c) we plot the energy gap between the $(2L+1)$th mode and the zero-energy mode, Δ, as a function of L. We find that Δ can be fitted as $\Delta \sim 1.564 L^{-0.485}$. Therefore, the spectrum is gapless around the zero energy. It is worth noting that, for the uniform flux case, the gapless spectrum is realized only when $\Phi = 0$, where the finite-energy bands exhibit the Dirac-like linear spectrum (see Appendix A).

We now turn to the features of the wave functions. In Fig. 4 we plot the probability density distribution for several values of ν. We focus on $1 \leqslant \nu \leqslant L+1$, i.e., the negative-energy sector. We find a rich structure of the eigenstates, depending on its eigenenergy. The most characteristic state is Fig. 4(d), where the wave function is compact and localized at the right edge. In fact, this is the right-edge mode whose eigenenergy is $-\sqrt{2}$ and whose exact wave function is shown in Appendix C. We label the annihilation operator of this edge mode as R_-; hereafter, the index $-$ stands for the negative-energy sector. Note that this edge mode is the same as that for the uniform π-flux case [42]. The remaining states are categorized into the following three types: (i) At the band edge [Figs. 4(a) and 4(f)], the wave functions are localized at the left edge. We call these modes the band-edge (BE) modes and we represent their annihilation operator by $X_{\nu,-}$. (ii) For the state with $E \sim -2$, which corresponds to the finite-energy flat band for the uniform π-flux case (Appendix D), the wave functions are sharply localized near the π-flux plaquette shown in Fig. 4(c). We call these modes the π-flux-localized (PFL) modes and represent their annihilation operators by $Y_{\nu,-}$. (iii) The intermediate states have moderate amplitudes on the left side of the system and a vanishingly small amplitude on the right side. The typical probability density distributions of the modes are shown in Figs. 4(b) and 4(e). We call these modes the intermediate (Int) modes and represent their annihilation operators by $Z_{\nu,-}$. Note that the origin of the PFL modes can be accounted for by the squared Hamiltonian, as we saw in the preceding section. Also, many of the sharply localized states tend to have a high weight in the right half of the system, since the hopping amplitude for h^A, $|t_{n,n+1}| = |1 + e^{i\Phi_n}|$, becomes smaller as n becomes larger.

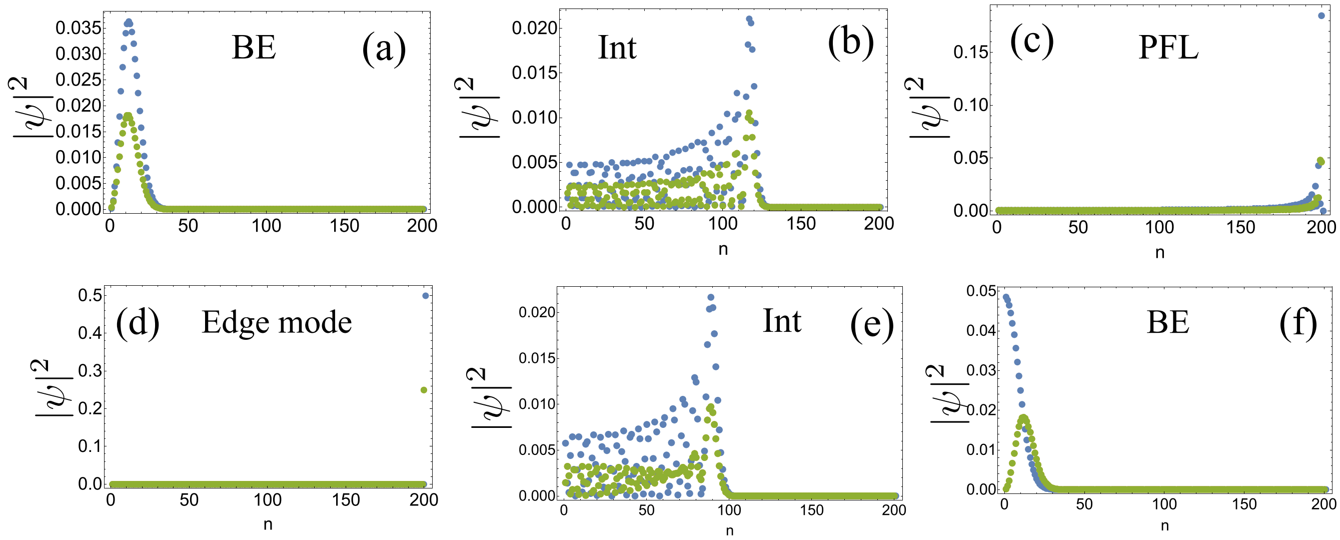

FIG. 4. Probability density distribution $|\psi^\nu(i)|$ for $(\Phi_{\rm min}, \Phi_{\rm max}) = (0, \pi)$, $L = 200$, and (a) $\nu = 1$, (b) $\nu = 30$, (c) $\nu = 100$, (d) $\nu = 164$, (e) $\nu = 184$, and (f) $\nu = 201$. The blue, orange, and green dots are for sublattices A, B, and C, respectively (the orange dots overlap the green ones). The corresponding eigenenergies are (a) -2.82, (b) -2.52, (c) -2.00, (d) $-\sqrt{2}$, (e) -1.00, and (f) -0.12.

Summarizing, we can explicitly write the structures of the eigenstates as

$$H = H_+ + H_-, \tag{9}$$

where

$$\begin{aligned} H_- = & -\sqrt{2}R_-^\dagger R_- + \sum_{\nu\in\mathrm{BE}} \varepsilon_\nu^{\mathrm{BE}} X_{\nu,-}^\dagger X_{\nu,-} \\ & + \sum_{\nu\in\mathrm{PFL}} \varepsilon_\nu^{\mathrm{PFL}} Y_{\nu,-}^\dagger Y_{\nu,-} + \sum_{\nu\in\mathrm{Int}} \varepsilon_\nu^{\mathrm{Int}} Z_{\nu,-}^\dagger Z_{\nu,-} \end{aligned} \tag{10}$$

represents the negative-energy part and H_+ is the chiral counterpart of H_- corresponding to the positive-energy part. Note that the degenerate zero-energy modes do not appear in the Hamiltonian. We remark that we do not specify a clear criterion for classifying X, Y, and Z since changes among them are crossoverlike rather than sharp deformations. The classification nevertheless gives useful insight for understanding the physical properties of this model, as we will argue in the following.

We next elucidate whether the above three types of states X, Y, and Z are localized or not. To this end, we investigate the scaling behavior of the inverse participation ratio (IPR), defined as

$$P_\nu = \sum_i |\psi^\nu(i)|^4. \tag{11}$$

In Fig. 5(a) we plot the IPR for the negative-energy sector for $L = 200$. Clearly, the compact right-edge mode has the largest IPR. The PFLs exhibit the secondary peak. The remaining states have small IPR, but the BE states have slightly larger IPR than the rest of the states. In Fig. 5(b) we plot the system-size dependence of the X, Y, and Z states. For all states, the IPR is fitted by the power function $P_\nu = xL^{-y}$. Again, as expected, the Z state has the largest exponent ($y = 0.865$), the X state has the second largest ($y = 0.496$), and the Y state exhibits the almost localized tendency ($y = 0.220$). From these results, it is quantitatively clear that the PFL states have a distinctively localized character compared with the remaining states.

Finally, we investigate the single-particle dynamics described by the unitary time evolution. Let $|\phi(0)\rangle$

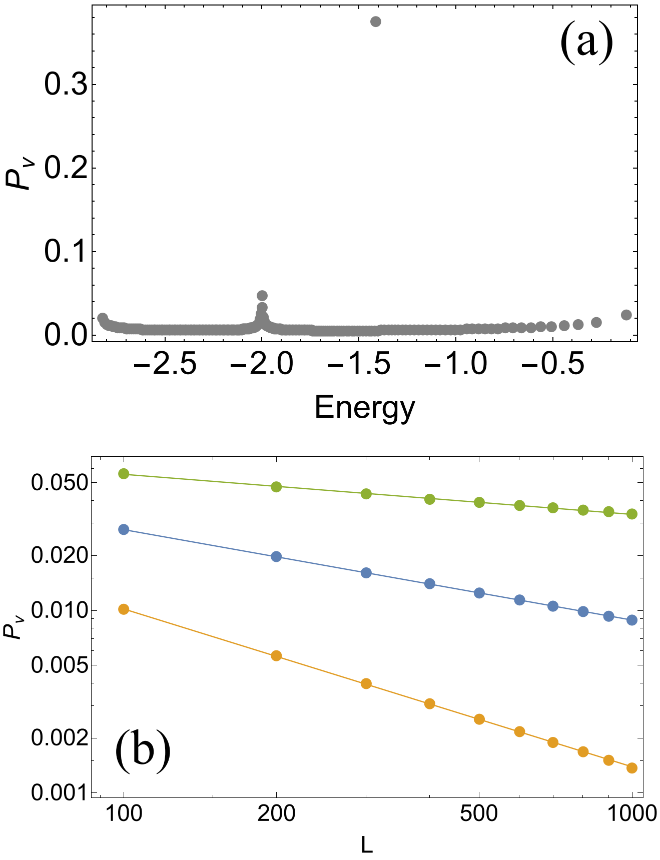

FIG. 5. (a) IPR for the negative-energy sector for $L = 200$. (b) L dependence of the IPR for $\nu = 1$ (blue dots), $\nu = (3/10)L$ (orange dots), and $\nu = L/2$ (green dots). The lines are the fitting curves.

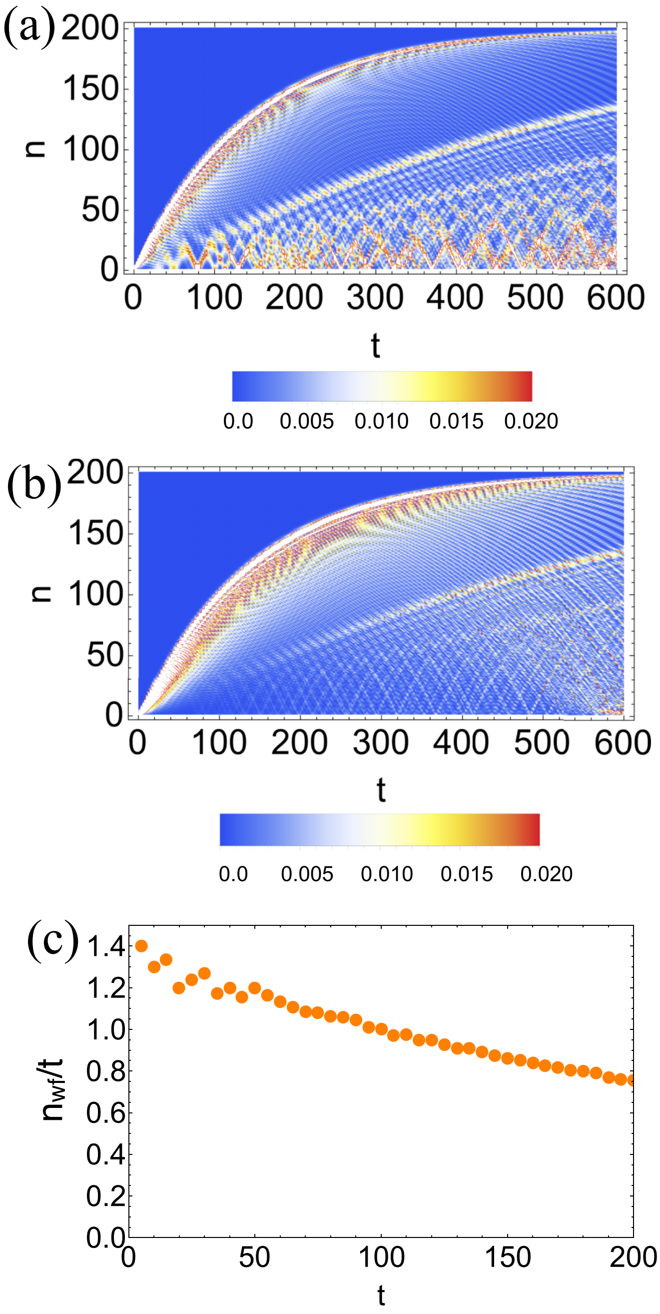

FIG. 6. Time evolution of the probability density distribution per unit cell for the initial condition (a) $\phi_{1,A}(0) = 1$ and (b) $\phi_{1,B}(0) = \phi_{1,C} = 1/\sqrt{2}$. (c) Coordinate of the wave front divided by time for (a).

be an initial state. Then, at the time t, the state is given as

$$|\phi(t)\rangle = e^{-iHt}\,|\phi(0)\rangle = \sum_{\nu} \varphi_{\nu}(t)\,|\nu\rangle\,, \tag{12}$$

$$\varphi_{\nu}(t) = \langle \nu\,|\phi(t)\rangle = \varphi_{\nu}(0)e^{-i\varepsilon_{\nu}t}, \tag{13}$$

where $|\nu\rangle := \alpha_{\nu}^{\dagger}\,|0\rangle$ ($|0\rangle$ represents the vacuum) and we set $\hbar = 1$.

In Fig. 6 we plot the time evolution of the probability density per unit cell,

$$N_n(t) = \begin{cases} |\phi_{A,n}(t)|^2 + |\phi_{B,n}(t)|^2 + |\phi_{C,n}(t)|^2, & 1 \leqslant n \leqslant L \\ |\phi_{A,n}(t)|^2, & n = L + 1, \end{cases} \tag{14}$$

with $\phi_i(t) = \langle i\,|\phi(t)\rangle = \langle 0|\,c_i\,|\phi(t)\rangle$. In Fig. 6(a) [Fig. 6(b)] we set the initial state as $\phi_{1,A}(0) = 1$ [$\phi_{1,B}(0) = \phi_{1,C}(0) = 1/\sqrt{2}$] and 0 otherwise. In other words, we set the initial states where the particle localizes at the left edge and see how the particle spreads in time evolution.

For both Figs. 6(a) and 6(b) we see a characteristic feature of the wave front, namely, for small t ($\lesssim$100), the wave front moves to the right. However, on approaching the right edge ($n \gtrsim 120$), it slows down and does not reach the right edge even after a very long time (to $t = 600$). In Fig. 6(c) we plot the coordinate of the wave front divided by time n_{wf}/t, where n_{wf} is the value of n at which $N_n(t)$ takes the maximal value. The initial state is the same as that for Fig. 6(a). We see that n_{wf}/t is a decreasing function of t, which clarifies the slowing down of the particle dynamics. This behavior is understood by the structure of the eigenstates, namely, as indicated in Eqs. (12) and (13), the overlap between the initial state and the eigenstates, $\phi_{\nu}(0)$, plays a decisive role in the quench dynamics. In the present case, the initial state has a very tiny overlap with the right-edge state and the PFL states. Since no eigenstate other than the right-edge state and the PFL states has a large weight near the right edge, the particle does not reach the right edge.

It is also worth noting that the degenerate zero modes do not affect the dynamics for Fig. 6(a) because these zero modes do not have an amplitude at A sites, meaning that the zero modes have zero overlap with the initial state. Considering the fact that the characteristic slowdown of the wave front is seen in both Figs. 6(a) and 6(b), we can conclude that this behavior does not originate from the degenerate zero modes.

B. Case of $(\Phi_{\min}, \Phi_{\max}) = (0, 2\pi)$

As another representative case, we study the case of $(\Phi_{\min}, \Phi_{\max}) = (0, 2\pi)$. It is worth noting that the flux distribution in this case satisfies $\Phi_n \equiv -\Phi_{L+1-n}$ (modulo 2π), which means that the right half of the system is the time-reversal counterpart of the left half.[1] The corresponding symmetry of the Hamiltonian is elaborated in Appendix E.

In Fig. 7(a) the energy spectrum for $L = 200$ is plotted. Remarkably, the energy spectrum looks quite similar to that of Fig. 3(a). However, there is a sharp difference from the previous case, that is, most of the finite-energy modes have (quasi)twofold degeneracy. To see this, focusing on the negative-energy modes, we plot $\delta\varepsilon_{\nu'}^{(1)} := \varepsilon_{2\nu'} - \varepsilon_{2\nu'-1}$ and $\delta\varepsilon_{\nu'}^{(2)} := \varepsilon_{2\nu'+1} - \varepsilon_{2\nu'}$ ($\nu' = 1, \ldots, L/2$). We see that $\delta\varepsilon_{\nu'}^{(1)}$ ($\delta\varepsilon_{\nu'}^{(2)}$) is almost zero for $\nu' \lesssim 50$ ($\nu' \gtrsim 50$). More precisely, setting the numerical threshold as $\eta' = 10^{-5}$, we obtain $\delta\varepsilon_{\nu'}^{(1)} < \eta'$ for $\nu' \leqslant 46$ and $\delta\varepsilon_{\nu'}^{(2)} < \eta'$ for $\nu' \geqslant 54$. Hence,

---

[1] Note that, when L is even, there is no plaquette exactly satisfying $\Phi_n = \pi$. Specifically, $\Phi_{L/2} = \pi\frac{L-2}{L-1}$ and $\Phi_{L/2+1} = \pi\frac{L}{L-1}$.

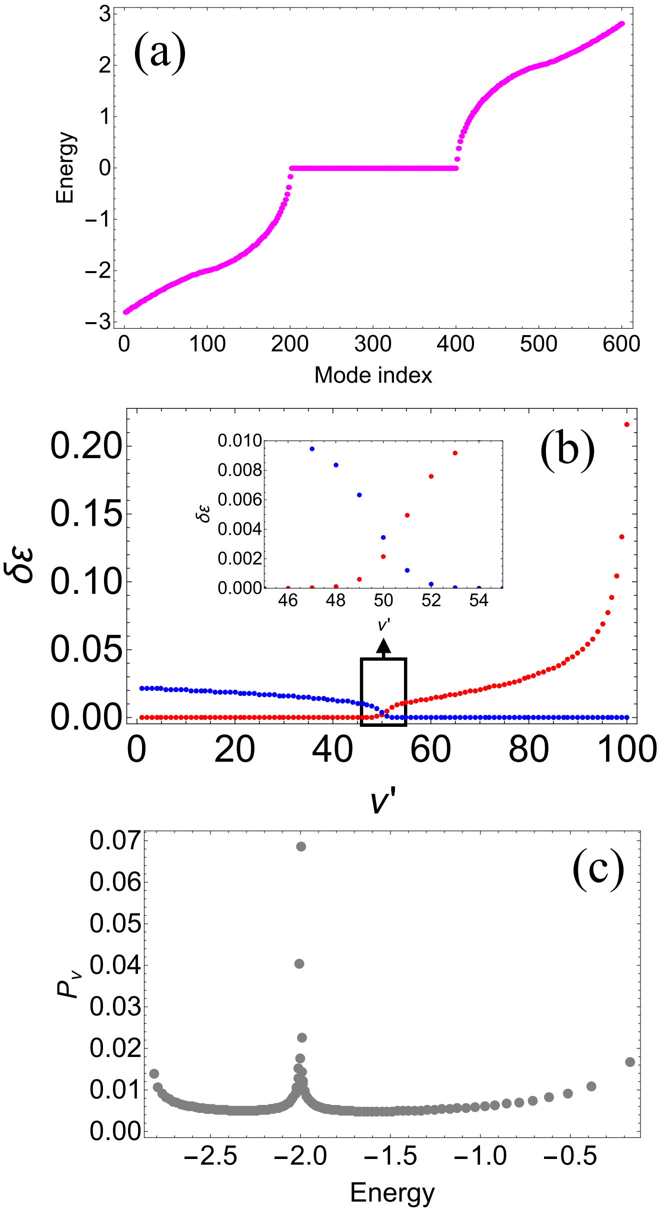

FIG. 7. Results for $L = 200$ and $(\Phi_{\mathrm{min}}, \Phi_{\mathrm{max}}) = (0, 2\pi)$. (a) Energy spectrum. (b) Energy gap between the neighboring eigenenergies (see the text for its definition). Red and blue dots represent $\delta\varepsilon^{(1)}_{\nu'}$ and $\delta\varepsilon^{(2)}_{\nu'}$, respectively. (c) IPR for the negative-energy sector.

as shown in the inset of Fig. 7(b), among the negative-energy modes ($\nu = 1, \dots, 201$), those with $\nu = 93, \dots, 107$ are nondegenerate while the other modes have twofold degeneracy within the numerical accuracy.

In Fig. 7(c) we plot the IPR for the negative-energy sector. Note that for a twofold-degenerate pair ν_1 and ν_2, the IPR is defined as

$$P_{(\nu_1,\nu_2)} = \sum_i \left(\frac{|\psi^{\nu_1}(i)|^2 + |\psi^{\nu_2}(i)|^2}{2} \right)^2 . \tag{15}$$

We again see a sharp peak near $E = -2$, which originates from the PFL states localized near $n = L/2$, i.e., the plaquettes with $\Phi_n \sim \pi$. We note that the edge state is absent in this configuration; hence the peak of the IPR at $E = -\sqrt{2}$ seen in Fig. 5(a) is absent.

In Figs. 8(a) and 8(b) we plot the time evolution of the probability density per unit cell for the same initial state as that for Figs. 6(a) and 6(b), respectively. Remarkably, for both cases, the particle starting from the left edge slows down as it approaches the center of the system and it does not reach the right half of the system.

We additionally consider the following two choices of the initial state. The first one is the case where the particle starts from the right edge [Fig. 8(c)]. We see that the particle does not reach the left half of the system. This behavior indicates that the PFL states obstruct the spreading of the particles, as is the case of $(\Phi_{\mathrm{min}}, \Phi_{\mathrm{max}}) = (0, \pi)$. The second one is the case where the particle starts from the center of the system corresponding to the portion of the nearly-π-flux plaquette [Fig. 8(d)]. We see that the spreading of the particle is highly suppressed for a long time, which is further evidence that the nearly-π-flux plaquette obstructs the particle dynamics.

C. Blocked dynamics due to the π-flux plaquette

From the results of Fig. 6 and Fig. 8, we see that the PFL states serve as a blockade over which the particle cannot spread. To further demonstrate this feature, we plot the time evolution of the probability density for the several combinations of $(\Phi_{\mathrm{min}}, \Phi_{\mathrm{max}})$ and the choices of the initial states.

In Figs. 9(a) and 9(b) we show the results for $(\Phi_{\mathrm{min}}, \Phi_{\mathrm{max}}) = (0, 1.5\pi)$, where the nearly-$\pi$-flux plaquette is located at $n \sim (2/3)L$, i.e., $n \sim 133$ for $L = 200$. As expected, the particle starting from the left (right) edge does not go across the opposite side separated by the π-flux plaquette, as shown in Fig. 9(a) [Fig. 9(b)]. In Fig. 9(c) we consider the case where $\Phi_{\mathrm{min}} \neq 0$. Note that the spectrum around the zero-energy modes is gapped, in contrast to the cases of $\Phi_{\mathrm{min}} = 0$. Clearly, the particle is again blocked by the π-flux plaquette, indicating that the blocking of the π-flux plaquette occurs regardless of the existence of the gap in the energy spectrum.

In Fig. 9(d) we consider the case of $(\Phi_{\mathrm{min}}, \Phi_{\mathrm{max}}) = (0, 4\pi)$, where there are two nearly-π-flux plaquettes at $n \sim L/4, (3/4)L$. We see that the particle starting at the middle of the two nearly-π-flux plaquettes is confined in the region between them.

Finally, in Fig. 9(e) we consider the case of $(\Phi_{\mathrm{min}}, \Phi_{\mathrm{max}}) = (0, 0.75\pi)$, which does not contain the π-flux plaquette, to clarify the essential role of the π-flux plaquette. We see that the blocked dynamics is not seen, namely, the wave front reaches the right edge around $t \sim 300$, though its velocity slightly decreases as it approaches the right edge.

From these results, the blocked dynamics due to the nearly-π-flux plaquettes and the corresponding PFL states around them is established.

IV. COMPARISON TO OTHER MODELS

In this section we show the results for two additional models with spatially increasing flux to make a comparison with the diamond-chain model.

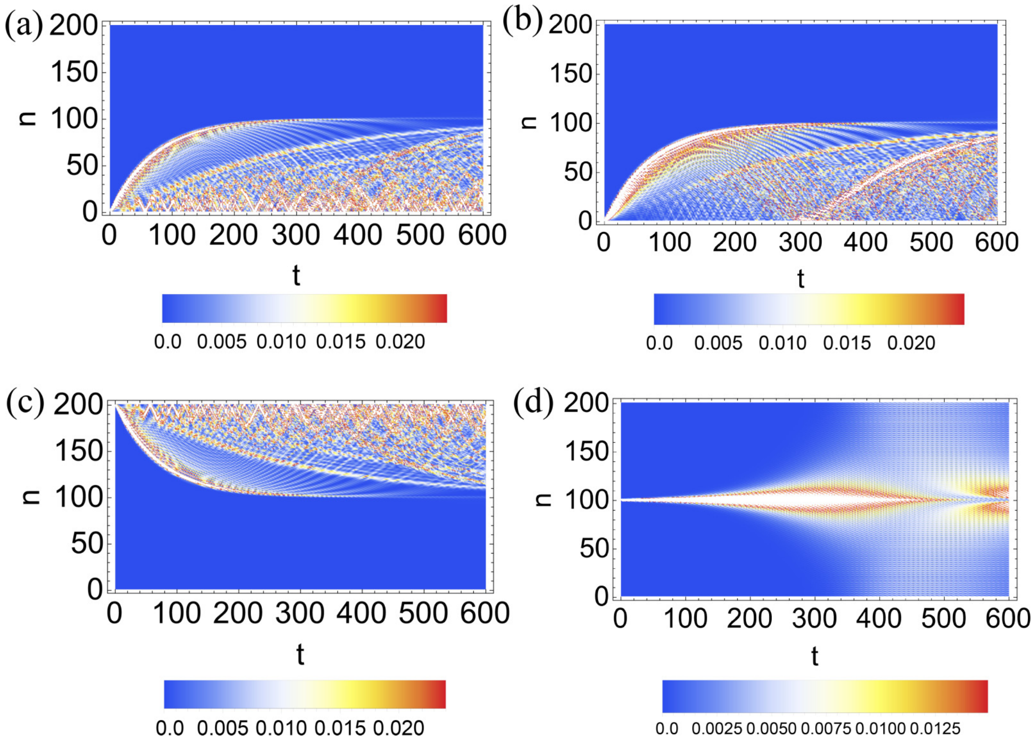

FIG. 8. Time evolution of the probability density distribution per unit cell for the initial condition (a) $\phi_{1,A}(0) = 1$, (b) $\phi_{1,B}(0) = \phi_{1,C} = 1/\sqrt{2}$, (c) $\phi_{L+1,A}(0) = 1$, and (d) $\phi_{L/2+1,A}(0) = 1$. We set $L = 200$ and $(\Phi_{\min}, \Phi_{\max}) = (0, 2\pi)$.

A. Creutz ladder

The Creutz ladder has a feature similar to the diamond-chain model, in that all bands, i.e., two bands in this case, become flat at a specific value of complex hopping [10,61–63]. It is also worth noting that the Creutz ladder is also realized in various artificial systems [64,65]. Here we consider a generalization of the Creutz ladder where the phase factors of the complex hoppings are spatially increasing as described in Fig. 10(a). Note that all bands become flat at $\Phi = \frac{\pi}{2}$ for the uniform case.

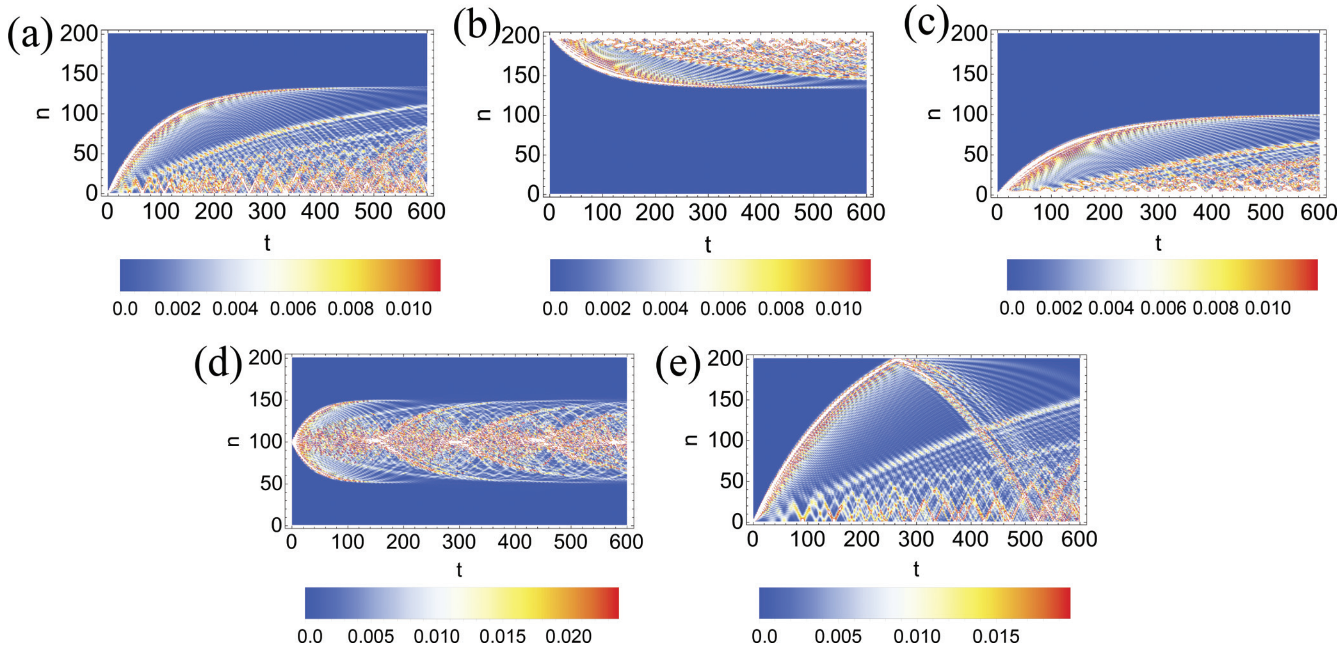

FIG. 9. Time evolution of the probability density distribution per unit cell for (a) $(\Phi_{\min}, \Phi_{\max}) = (0, 1.5\pi)$ and $\phi_{1,A}(0) = 1$, (b) $(\Phi_{\min}, \Phi_{\max}) = (0, 1.5\pi)$ and $\phi_{L+1,A}(0) = 1$, (c) $(\Phi_{\min}, \Phi_{\max}) = (0.5\pi, 1.5\pi)$ and $\phi_{1,A}(0) = 1$, (d) $(\Phi_{\min}, \Phi_{\max}) = (0, 4\pi)$ and $\phi_{L/2,A}(0) = 1$, and (e) $(\Phi_{\min}, \Phi_{\max}) = (0, 0.75\pi)$ and $\phi_{1,A}(0) = 1$. The system size is $L = 200$.

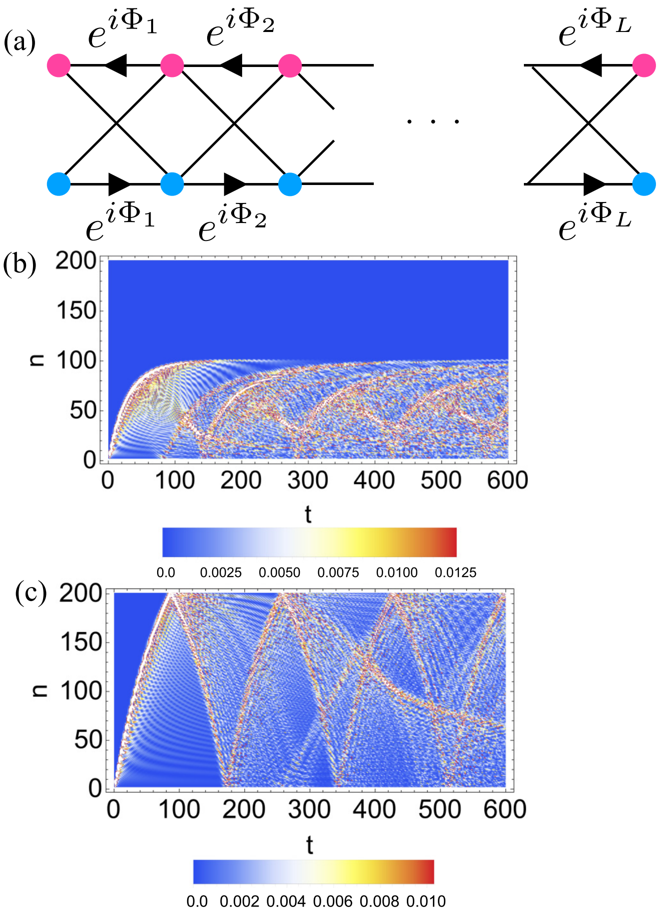

FIG. 10. (a) Schematic of the Creutz ladder with spatially increasing phase factors. The time evolution of the probability density distribution per unit cell is shown for (b) $(\Phi_{\rm min}, \Phi_{\rm max}) = (0, \pi)$ and $\phi_{n=1,u}(0) = 1$ and (c) $(\Phi_{\rm min}, \Phi_{\rm max}) = (0, 0.3\pi)$ and $\phi_{n=1,u}(0) = 1$. Note that n labels the column and the subscript u stands for the upper row. We set $L = 200$ [the number of sites is $2(L + 1) = 402$].

In Fig. 10(b) we show the particle dynamics for $(\Phi_{\rm min}, \Phi_{\rm max}) = (0, \pi)$. Clearly, the particle slows down as approaching $n \sim L/2$, where the value of the phase factor is close to that of the case of all bands flat, exhibiting similarity to the diamond chain. For comparison, we also consider the case of $(\Phi_{\rm min}, \Phi_{\rm max} = 0, 0.3\pi)$ [Fig. 10(c)], where none of the phase factors corresponds to the case of all bands flat. In this case, the blocking of the particle does not occur and it reaches the right edge, which also resembles the result of the diamond chain.

B. Two-leg ladder

We next consider the two-leg ladder model with a magnetic flux [Fig. 11(a)]. In contrast to the diamond chain and Creutz lattice, in the uniform case, the complete flat bands do not appear at any value of the flux. It is worth noting that the model with uniform flux has been studied as the thinnest limit of the Hofstadter model [66–68].

In Figs. 11(b) and 11(c) we show the particle dynamics starting from the left edge for $(\Phi_{\rm min}, \Phi_{\rm max}) = (0, \pi)$ and $(\Phi_{\rm min}, \Phi_{\rm max}) = (0, 2\pi)$, respectively. In Fig. 11(b) the particle exhibits the standard spreading dynamics, reaching the right edge after a certain time, and the reflected wave arises, as expected. Meanwhile, in Fig. 11(c) the particle sharply slows down around $n \sim 130$, similar to the diamond chain and the Creutz ladder. This behavior is nontrivial because the sharply localized eigenstates are expected to arise for any value of flux. For further comparison, we show the particle dynamics with the initial position being the middle of the system in Fig. 11(d). We see that the blocking of the particle dynamics is much weaker than the diamond-chain case and not a few amounts of the particle density propagate to the left and right edges. Combining these results, we speculate that there can be a universal, i.e., lattice-independent, mechanism of the blocking dynamics by the spatially increasing flux even without the localized wave functions unique to the all-flat-band systems, but the degree of blocking is not as strong as that of the all-flat-band systems such as the diamond chain and the Creutz ladder. Further studies on a possible mechanism are necessary to extract the uniqueness of the lattices with all bands flat.

C. Early-time dynamics

We further make a comparison among three models from a different point of view, namely, we focus on the early-time dynamics for each model. The study of particle or correlation spreading is interesting since real experiments can capture such a spreading. For example, a recent optical lattice experiment [69] observed the spread of correlation between a doublon and holon in a quench dynamics and found a linearlike propagation of it. Also, a cloud spreading has been investigated in detail [70]. Some theoretical works about quench dynamics of particle spreading in early time have been reported [71,72]. Motivated by these works, we focus on the early-time dynamics of the flat-band and the non-flat-band models. Several behaviors are observed from our numerical results.

(i) In the flat-band model with linearly increasing flux $(\Phi_{\rm min}, \Phi_{\rm max}) = (0, \pi)$ [as shown in Fig. 6(a)], its dynamics does not exhibit the linear spreading. We expect that such a dynamics occurs for an initial particle put on any position.

(ii) In the two-leg ladder model with linearly increasing $(\Phi_{\rm min}, \Phi_{\rm max}) = (0, \pi)$, linearlike spreading in $0 \leqslant t \leqslant 150$ is observed for an initial particle put on any position [as shown in Fig. 11(b)].

(iii) For the two-leg ladder model with an initial position being the left end, the secondary wave front is strongly suppressed [the blue regions within $0 \leqslant t \leqslant 200$ and $0 \leqslant n \leqslant 50$ of Fig. 11(b) and $0 \leqslant t \leqslant 100$ and $0 \leqslant n \leqslant 20$ of Fig. 11(c)], which is in contrast to the diamond chain. This might originate from the chiral nature of the dynamics.

(iv) In the two-leg ladder model with linearly increasing $(\Phi_{\rm min}, \Phi_{\rm max}) = (0, 2\pi)$, when the initial particle is set around the π flux, the particle matter wave clearly exhibits a linear wave front [Fig. 11(d)]. This is significantly different from that of the flat-band case, where the initial particle is not spread, highly bounded around the π flux as shown in Fig. 8(d).

In particular, observation (iv) implies that a highly localized eigenstate around the π-flux plaquette is absent

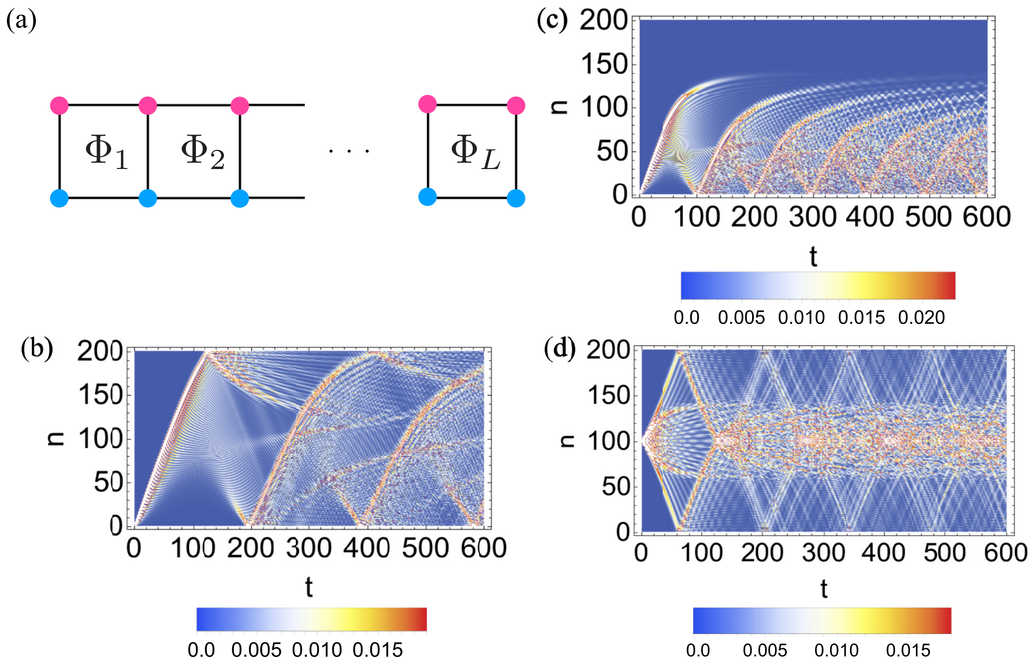

FIG. 11. (a) Schematic of the two-leg ladder with spatially increasing flux. The time evolution of the probability density distribution per unit cell is shown for (b) $(\Phi_{\min}, \Phi_{\max}) = (0, \pi)$ and $\phi_{n=1,u}(0) = 1$, (c) $(\Phi_{\min}, \Phi_{\max}) = (0, 2\pi)$ and $\phi_{n=1,u}(0) = 1$, and (d) $(\Phi_{\min}, \Phi_{\max}) = (0, 2\pi)$ and $\phi_{n=L/2+1,u}(0) = 1$. Note that n labels the column and the subscript u (l) stands for the upper (lower) row. We set $L = 200$ [the number of sites is $2(L + 1) = 402$].

in the two-leg ladder model, which is in contrast to the flat-band models where the nonspreading dynamics is attributed to the highly localized eigenstates [73]. These behaviors, in particular, the difference between the flat-band model and conventional dispersive band models, can be observed in a real experiment such as photonic waveguides.

V. CONCLUSION

We have investigated the characteristic structures of the eigenstates and resulting dynamics in the diamond-chain model with spatially increasing flux. For the uniform flux case, the remarkable feature of the diamond-chain model is the realization of the all-flat-band system at the π flux. This feature carries over to the spatially-increasing-flux case, in that the sharply localized eigenstates emerge around the π-flux plaquette. Consequently, the π-flux plaquette serves as a blockade of the particle dynamics. Indeed, by investigating the particle dynamics with the localized eigenstates, we find that the particle slows down as it approaches the π-flux plaquette. This behavior of the particle dynamics is unique to the present model, which does not resemble any of the conventional spreading dynamics for itinerant systems, the Bloch oscillation for the Wannier-Stark-type localized systems, or the complete localization for the Aharonov-Bohm cages.

We conclude this paper by addressing future directions for research. As for the single-particle dynamics, various patterns of spatially varying flux, such as a random flux or quasiperiodic flux, will be sources of unconventional features, which we think are worth being studied. The investigation of eigenstate properties of the squared Hamiltonian would provide insight to help us understand the localization properties of the eigenstates of the original model. Considering the many-particle system under the present setup is another interesting direction because the π-flux blockade serves as a novel mechanism of confining a particle which will lead to slow thermalization or disorder-free localization. Finally, the experimental realization of the present model will also be an important issue. The photonic waveguides [41,42] and ultracold atoms [18,74] will be possible platforms due to the tunability of the effective magnetic flux. For instance, Ref. [41] has suggested that the tight-binding model on the diamond chain with flux is realized as an effective Hamiltonian of the periodically driven photonic waveguide, and the phase factor can be locally determined by the phase modulation of the driving term on each site. Hence, the spatially dependent flux can be realized by tuning the site-dependent phase. Quite recently, the electric circuit realization of the π-flux diamond chain was also reported [46], which may offer another platform for the experimental realization of our model.

ACKNOWLEDGMENTS

This work was supported by JST CREST Grant No. JPMJCR19T1 and by JSPS KAKENHI Grants No. JP23K03243 (T.M.), No. JP23H01091 (Y.H.), and No. JP23K13026 (Y.K.).

APPENDIX A: BULK SPECTRUM OF THE DIAMOND CHAIN WITH FLUX

In this Appendix we review the bulk spectrum of the diamond chain in the presence of the uniform flux Φ. For the uniform flux, the transitional invariance is preserved; hence we use the momentum-space description. The Bloch

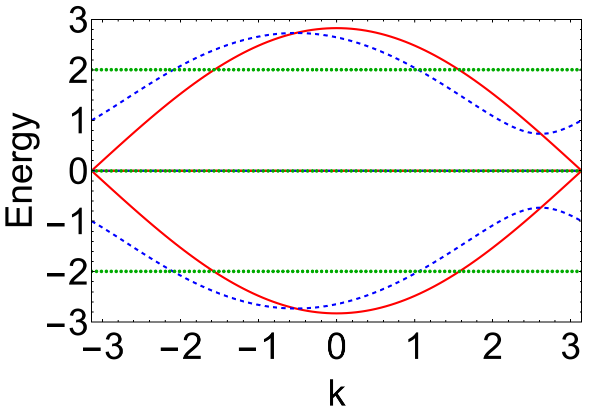

FIG. 12. Band structure for the diamond-chain model with uniform flux. The red solid, blue dashed, and green dotted lines are for $\Phi = 0, \pi/3$, and π, respectively.

Hamiltonian reads

$$H(k) = \begin{pmatrix} 0 & 1+e^{-i(k+\Phi)} & 1+e^{-ik} \\ 1+e^{i(k+\Phi)} & 0 & 0 \\ 1+e^{ik} & 0 & 0 \end{pmatrix}. \quad \text{(A1)}$$

As mentioned in the main text, the model preserves the chiral symmetry. In the momentum-space picture, this symmetry can be represented by $\bar{g}H(k)\bar{g} = -H(k)$, where $\bar{g} = \mathrm{diag}(1, -1, -1)$. Since $|\mathrm{Tr}(\bar{g})| = 1$, there exists a zero-energy mode for any k.

The dispersion relation can be obtained analytically by again taking the square of the Hamiltonian

$$H^2(k) = \begin{pmatrix} |f_1(k)|^2 + |f_2(k)|^2 & 0 & 0 \\ 0 & |f_1(k)|^2 & f_1^*(k)f_2(k) \\ 0 & f_1(k)f_2^*(k) & |f_2(k)|^2 \end{pmatrix}, \quad \text{(A2)}$$

where $f_1(k) = 1 + e^{-i(k+\Phi)}$ and $f_2(k) = 1 + e^{-ik}$. We can easily find from Eq. (A2) that the eigenenergies of $H^2(k)$ are 0 and $|f_1(k)|^2 + |f_2(k)|^2$ (doubly degenerate). Consequently, the eigenenergies and the eigenvectors of $H(k)$ are given as

$$E_\pm(k) = \pm\sqrt{|f_1(k)|^2 + |f_2(k)|^2},$$

$$\boldsymbol{u}_{k,\pm} = \frac{1}{\sqrt{2[|f_1(k)|^2 + |f_2(k)|^2]}} \begin{pmatrix} \sqrt{|f_1(k)|^2 + |f_2(k)|^2} \\ \pm f_1^*(k) \\ \pm f_2^*(k) \end{pmatrix}, \quad \text{(A3a)}$$

$$E_0(k) = 0, \quad \boldsymbol{u}_{k,0} = \frac{1}{\sqrt{|f_1(k)|^2 + |f_2(k)|^2}} \begin{pmatrix} 0 \\ f_2(k) \\ -f_1(k) \end{pmatrix}. \quad \text{(A3b)}$$

It should be noted that at $\Phi = \pi$ we have $E_\pm(k) = \pm 2$ for any k, which means that all bands are flat in this case. In Fig. 12 we plot the band structures for $\Phi = 0$ (red solid lines), $\pi/3$ (blue dashed lines), and π (green dotted lines).

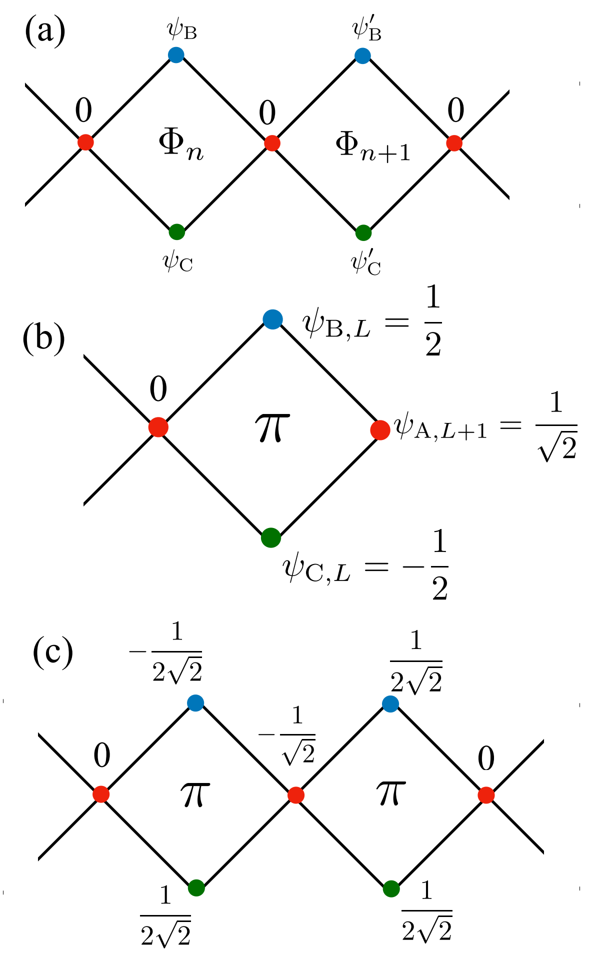

FIG. 13. Schematics of (a) the CLS with $E = 0$, (b) the right-edge state, and (c) the CLS with $E = -2$ for the uniform π flux.

APPENDIX B: COMPACT LOCALIZED STATE AT $E = 0$

In this Appendix we elucidate the compact localized state (CLS) at $E = 0$. The guiding principle of constructing the CLS is to set the amplitudes at A sites to be zero. For the configuration of Fig. 13(a), we obtain the compact wave function with finite amplitudes on only four sites. For its solution, the above assumption leads to the three equations

$$\psi_B + \psi_C = 0, \quad \text{(B1a)}$$

$$e^{-i\Phi_n}\psi_B + \psi_C + \psi'_B + \psi'_C = 0, \quad \text{(B1b)}$$

and

$$e^{-i\Phi_{n+1}}\psi'_B + \psi'_C = 0. \quad \text{(B1c)}$$

From these equations, we obtain the wave function of the CLS,

$$(\psi_B, \psi_C, \psi'_B, \psi'_C) = \frac{1}{\mathcal{N}}\left(1, -1, -\frac{x_1}{x_2}, e^{-i\Phi_{n+1}}\frac{x_1}{x_2}\right), \quad \text{(B2)}$$

where $\mathcal{N}$ is the normalization factor, $x_1 = e^{-i\Phi_n} - 1$, and $x_2 = 1 - e^{-i\Phi_{n+1}}$. It is worth noting that the CLSs in general are not orthogonal to each other, since the neighboring CLSs overlap. We also note that the solution is not valid when $\Phi_{n+1} = 0$

because $x_2 = 0$. In fact, in this case, the CLS is given as

$$(\psi_B, \psi_C, \psi_B', \psi_C') = \frac{1}{\sqrt{2}}(0, 0, 1, -1), \tag{B3}$$

which indicates that the CLS has finite amplitude on only two sites rather than four sites.

APPENDIX C: RIGHT-EDGE STATE FOR $\Phi_{\max} = \pi$

Here we discuss the right-edge state for $\Phi_{\max} = \pi$. For the uniform π-flux model, the compact edge states with the eigenenergy $\pm\sqrt{2}$ appear [42]. Due to the compact nature, we have the same edge states even in the present case of the increasing flux with $\Phi_{\max} = \pi$. To be specific, for the configuration of Fig. 13(b), the right-edge state has finite amplitudes at only three sites, i.e., (B, L), (C, L), and $(A, L+1)$. For the eigenstate with $E = -\sqrt{2}$, the wave function is given as

$$(\psi_{A,L+1}, \psi_{B,L}, \psi_{C,L}) = \left(\frac{1}{\sqrt{2}}, \frac{1}{2}, -\frac{1}{2}\right). \tag{C1}$$

APPENDIX D: FINITE-ENERGY CLS FOR π FLUX

As mentioned in Appendix A, the case of the uniform flux with $\Phi = \pi$ is special in that all bands are completely flat. Therefore, the states with $E = \pm 2$ can also be given by the set of CLSs. In Fig. 13(c) we present the wave function for $E = -2$, which can be obtained by solving the Schrödinger equation explicitly.

APPENDIX E: SYMMETRY OF THE HAMILTONIAN FOR $(\Phi_{\min}, \Phi_{\max}) = (0, 2\pi)$

We now discuss the symmetry of the Hamiltonian for the case of $(\Phi_{\min}, \Phi_{\max}) = (0, 2\pi)$ and L is even. The Hamiltonian $\mathcal{H}$ satisfies the relation

$$\mathcal{P}\mathcal{H}\mathcal{P}^{-1} = \mathcal{H}, \tag{E1}$$

where

$$[\mathcal{P}]_{(n,a),(m,a')} = \begin{cases} 1 & \text{for } m = R_A(n),\ a = a' = A \\ e^{i\Phi_n} & \text{for } m = R_B(n),\ a = a' = B \\ 1 & \text{for } m = R_C(n),\ a = a' = C \\ 0 & \text{otherwise,} \end{cases} \tag{E2}$$

with $R_A(n) = L + 2 - n$ and $R_B(n) = R_C(n) = L + 1 - n$.

Let us discuss the consequence of this symmetry on the dynamics. To be specific, we consider the case corresponding to Fig. 8(d), where $\phi_{L/2+1,A}(0) = 1$. In this case, the initial state is at the center of the system. Noting that $P\,|\phi(0)\rangle = P^{-1}\,|\phi(0)\rangle = |\phi(0)\rangle$, where P denotes the operator represented by the matrix $\mathcal{P}$, we have

$$\begin{aligned}\phi_{(n,a)}(t) &= \langle (n,a)|\,|\phi(t)\rangle \\ &= \langle (n,a)|\, e^{-iHt}\,|\phi(0)\rangle \\ &= \langle (n,a)|\, Pe^{-iHt}P^{-1}\,|\phi(0)\rangle \\ &= e^{i\chi_{(n,a)}}\langle (R_a(n), a)\,|\phi(t)\rangle\,,\end{aligned} \tag{E3}$$

where we have used $\langle (n,a)|\,P = e^{i\chi_{(n,a)}}\,\langle (R_a(n), a)|$ with the phase factor $\chi_{(n,a)}$ being determined by Eq. (E2). This leads to the relation $|\phi_{(n,a)}(t)| = |\phi_{(R_a(n),a)}(t)|$, which means that the particle density spreads in a symmetric manner. We note, however, that $N_n(t)$ plotted in Fig. 8(d) is not exactly symmetric with respect to $n = L/2 + 1$ because the definition of Eq. (14) is not symmetric.

---

[1] Y. Hatsugai and A. Sugi, Int. J. Mod. Phys. B **15**, 2045 (2001).
[2] L. Mazza, M. Aidelsburger, H.-H. Tu, N. Goldman, and M. Burrello, New J. Phys. **17**, 105001 (2015).
[3] E. J. Meier, F. A. An, and B. Gadway, Nat. Commun. **7**, 13986 (2016).
[4] C. Wang, P. Zhang, X. Chen, J. Yu, and H. Zhai, Phys. Rev. Lett. **118**, 185701 (2017).
[5] F. Cardano, A. D'Errico, A. Dauphin, M. Maffei, B. Piccirillo, C. de Lisio, G. De Filippis, V. Cataudella, E. Santamato, L. Marrucci, M. Lewenstein, and P. Massignan, Nat. Commun. **8**, 15516 (2017).
[6] Z. Gong and M. Ueda, Phys. Rev. Lett. **121**, 250601 (2018).
[7] L. Zhang, L. Zhang, and X.-J. Liu, Phys. Rev. A **99**, 053606 (2019).
[8] M. Maffei, A. Dauphin, F. Cardano, M. Lewenstein, and P. Massignan, New J. Phys. **20**, 013023 (2018).
[9] A. Haller, P. Massignan, and M. Rizzi, Phys. Rev. Res. **2**, 033200 (2020).
[10] Y. Kuno, T. Mizoguchi, and Y. Hatsugai, Phys. Rev. A **102**, 063325 (2020).
[11] T. Mizoguchi, Y. Kuno, and Y. Hatsugai, Phys. Rev. Lett. **126**, 016802 (2021).
[12] M. Heyl, A. Polkovnikov, and S. Kehrein, Phys. Rev. Lett. **110**, 135704 (2013).
[13] S. Vajna and B. Dóra, Phys. Rev. B **91**, 155127 (2015).
[14] R. Okugawa, H. Oshiyama, and M. Ohzeki, Phys. Rev. Res. **3**, 043064 (2021).
[15] D. Jaksch, C. Bruder, J. I. Cirac, C. W. Gardiner, and P. Zoller, Phys. Rev. Lett. **81**, 3108 (1998).
[16] D. Jaksch and P. Zoller, New J. Phys. **5**, 56 (2003).
[17] M. Lewenstein, A. Sanpera, V. Ahufinger, B. Damski, A. Sen(De), and U. Sen, Adv. Phys. **56**, 243 (2007).
[18] I. Bloch, J. Dalibard, and W. Zwerger, Rev. Mod. Phys. **80**, 885 (2008).
[19] J. D. Joannopoulos, P. R. Villeneuve, and S. Fan, Nature (London) **386**, 143 (1997).
[20] T. Ozawa, H. M. Price, A. Amo, N. Goldman, M. Hafezi, L. Lu, M. C. Rechtsman, D. Schuster, J. Simon, O. Zilberberg, and I. Carusotto, Rev. Mod. Phys. **91**, 015006 (2019).
[21] C. L. Kane and T. C. Lubensky, Nat. Phys. **10**, 39 (2014).
[22] G. Ma, M. Xiao, and C. T. Chan, Nat. Rev. Phys. **1**, 281 (2019).
[23] P. W. Anderson, Phys. Rev. **109**, 1492 (1958).
[24] E. Abrahams, P. W. Anderson, D. C. Licciardello, and T. V. Ramakrishnan, Phys. Rev. Lett. **42**, 673 (1979).

[25] F. Evers and A. D. Mirlin, Rev. Mod. Phys. **80**, 1355 (2008).
[26] G. H. Wannier, Phys. Rev. **117**, 432 (1960).
[27] M. Atala, M. Aidelsburger, J. T. Barreiro, D. Abanin, T. Kitagawa, E. Demler, and I. Bloch, Nat. Phys. **9**, 795 (2013).
[28] T. Kohlert, S. Scherg, P. Sala, F. Pollmann, B. Hebbe Madhusudhana, I. Bloch, and M. Aidelsburger, Phys. Rev. Lett. **130**, 010201 (2023).
[29] L.-K. Lim, J.-N. Fuchs, and G. Montambaux, Phys. Rev. Lett. **108**, 175303 (2012).
[30] R. Khomeriki and S. Flach, Phys. Rev. Lett. **116**, 245301 (2016).
[31] M. Di Liberto, N. Goldman, and G. Palumbo, Nat. Commun. **11**, 5942 (2020).
[32] S. Kitamura, N. Nagaosa, and T. Morimoto, Commun. Phys. **3**, 63 (2020).
[33] J. Vidal, R. Mosseri, and B. Douçot, Phys. Rev. Lett. **81**, 5888 (1998).
[34] J. Vidal, B. Douçot, R. Mosseri, and P. Butaud, Phys. Rev. Lett. **85**, 3906 (2000).
[35] J. Vidal, P. Butaud, B. Douçot, and R. Mosseri, Phys. Rev. B **64**, 155306 (2001).
[36] B. Douçot and J. Vidal, Phys. Rev. Lett. **88**, 227005 (2002).
[37] R. Mosseri, R. Vogeler, and J. Vidal, Phys. Rev. B **106**, 155120 (2022).
[38] A. Ahmed, A. Ramachandran, I. M. Khaymovich, and A. Sharma, Phys. Rev. B **106**, 205119 (2022).
[39] A. R. Kolovsky, P. S. Muraev, and S. Flach, Phys. Rev. A **108**, L010201 (2023).
[40] A. M. Marques, J. Mögerle, G. Pelegrí, S. Flannigan, R. G. Dias, and A. J. Daley, Phys. Rev. Res. **5**, 023110 (2023).
[41] S. Mukherjee, M. Di Liberto, P. Öhberg, R. R. Thomson, and N. Goldman, Phys. Rev. Lett. **121**, 075502 (2018).
[42] M. Kremer, I. Petrides, E. Meyer, M. Heinrich, O. Zilberberg, and A. Szameit, Nat. Commun. **11**, 907 (2020).
[43] G. Cáceres-Aravena, D. Guzmán-Silva, I. Salinas, and R. A. Vicencio, Phys. Rev. Lett. **128**, 256602 (2022).
[44] H. Li, Z. Dong, S. Longhi, Q. Liang, D. Xie, and B. Yan, Phys. Rev. Lett. **129**, 220403 (2022).
[45] J. G. Martinez, C. S. Chiu, B. M. Smitham, and A. A. Houck, Sci. Adv. **9**, eadj7195 (2023).
[46] W. Zhang, H. Wang, H. Sun, and X. Zhang, Phys. Rev. Lett. **130**, 206401 (2023).
[47] C. Chase-Mayoral, L. Q. English, N. Lape, Y. Kim, S. Lee, A. Andreanov, S. Flach, and P. Kevrekidis, Phys. Rev. B **109**, 075430 (2024).
[48] B. Sutherland, Phys. Rev. B **34**, 5208 (1986).
[49] E. H. Lieb, Phys. Rev. Lett. **62**, 1201 (1989).
[50] P. W. Brouwer, E. Racine, A. Furusaki, Y. Hatsugai, Y. Morita, and C. Mudry, Phys. Rev. B **66**, 014204 (2002).
[51] M. Koshino, T. Morimoto, and M. Sato, Phys. Rev. B **90**, 115207 (2014).
[52] J. W. McClure, Phys. Rev. **104**, 666 (1956).
[53] J. Arkinstall, M. H. Teimourpour, L. Feng, R. El-Ganainy, and H. Schomerus, Phys. Rev. B **95**, 165109 (2017).
[54] J. Attig and S. Trebst, Phys. Rev. B **96**, 085145 (2017).
[55] T. Mizoguchi, Y. Kuno, and Y. Hatsugai, Phys. Rev. A **102**, 033527 (2020).
[56] T. Mizoguchi, T. Yoshida, and Y. Hatsugai, Phys. Rev. B **103**, 045136 (2021).
[57] T. Yoshida, T. Mizoguchi, Y. Kuno, and Y. Hatsugai, Phys. Rev. B **103**, 235130 (2021).
[58] L. A. Navarro-Labastida and G. G. Naumis, Phys. Rev. B **107**, 155428 (2023).
[59] D. Matsumoto, T. Mizoguchi, and Y. Hatsugai, J. Phys. Soc. Jpn. **92**, 034705 (2023).
[60] T. Mizoguchi and Y. Hatsugai, Phys. Rev. B **107**, 094201 (2023).
[61] M. Creutz, Phys. Rev. Lett. **83**, 2636 (1999).
[62] M. Creutz, Rev. Mod. Phys. **73**, 119 (2001).
[63] Y. Kuno, T. Orito, and I. Ichinose, New J. Phys. **22**, 013032 (2020).
[64] H. Alaeian, C. W. S. Chang, M. V. Moghaddam, C. M. Wilson, E. Solano, and E. Rico, Phys. Rev. A **99**, 053834 (2019).
[65] J. S. C. Hung, J. H. Busnaina, C. W. S. Chang, A. M. Vadiraj, I. Nsanzineza, E. Solano, H. Alaeian, E. Rico, and C. M. Wilson, Phys. Rev. Lett. **127**, 100503 (2021).
[66] D. Hügel and B. Paredes, Phys. Rev. A **89**, 023619 (2014).
[67] S. Mugel, A. Dauphin, P. Massignan, L. Tarruell, M. Lewenstein, C. Lobo, and A. Celi, SciPost Phys. **3**, 012 (2017).
[68] M. E. Tai, A. Lukin, M. Rispoli, R. Schittko, T. Menke, D. Borgnia, P. M. Preiss, F. Grusdt, A. M. Kaufman, and M. Greiner, Nature (London) **546**, 519 (2017).
[69] M. Cheneau, P. Barmettler, D. Poletti, M. Endres, P. Schauß, T. Fukuhara, C. Gross, I. Bloch, C. Kollath, and S. Kuhr, Nature (London) **481**, 484 (2012).
[70] J. P. Ronzheimer, M. Schreiber, S. Braun, S. S. Hodgman, S. Langer, I. P. McCulloch, F. Heidrich-Meisner, I. Bloch, and U. Schneider, Phys. Rev. Lett. **110**, 205301 (2013).
[71] A. Jreissaty, J. Carrasquilla, and M. Rigol, Phys. Rev. A **88**, 031606(R) (2013).
[72] L. Vidmar, S. Langer, I. P. McCulloch, U. Schneider, U. Schollwöck, and F. Heidrich-Meisner, Phys. Rev. B **88**, 235117 (2013).
[73] D. Leykam, A. Andreanov, and S. Flach, Adv. Phys.: X **3**, 1473052 (2018).
[74] M. Aidelsburger, M. Atala, S. Nascimbène, S. Trotzky, Y.-A. Chen, and I. Bloch, Phys. Rev. Lett. **107**, 255301 (2011).